



CHORUS

This is the accepted manuscript made available via CHORUS. The article has been published as:

Superexchange-induced valley splitting in two-dimensional transition metal dichalcogenides: A first-principles study for rational design

E. A. Peterson, J. B. Haber, and J. B. Neaton

Phys. Rev. B **104**, 205421 — Published 15 November 2021

DOI: [10.1103/PhysRevB.104.205421](https://doi.org/10.1103/PhysRevB.104.205421)

Superexchange-induced valley splitting in two-dimensional transition metal dichalcogenides: a first-principles study for rational design

E.A. Peterson,^{1,2} J.B. Haber,¹ and J.B. Neaton^{1,3,4}

¹*Department of Physics, University of California Berkeley, Berkeley, CA 94720, USA*

²*Chemical Science Division, Lawrence Berkeley National Laboratory, Berkeley, CA 94720, USA*

³*Materials Science Division, Lawrence Berkeley National Laboratory, Berkeley, CA 94720, USA*

⁴*Kavli Energy Nanosciences Institute, Berkeley, CA 94720, USA*

(Dated: November 2, 2021)

Monolayer transition metal dichalcogenides (TMDs) with spin-valley coupling are a well-studied class of two-dimensional materials with potential for novel optoelectronics applications. Breaking time reversal symmetry via an external magnetic field or supporting magnetic substrate can lift the degeneracy of the band gaps at the inequivalent K and K' high symmetry points, or valleys, in the monolayer TMD Brillouin zone, a phenomenon known as valley splitting. However, reported valley splittings thus far are modest, and a detailed structural and chemical understanding of valley splitting via magnetic substrates is lacking. Here we probe the underlying physical mechanism with a series of density functional theory (DFT) calculations of magnetic atoms with varying coverage on the surface of prototypical monolayer WSe_2 and MoS_2 TMDs. Near-valence band edge energies for variable magnetic atom height, lateral registry, and magnetic moment are calculated with DFT, and trends are rationalized with a model Hamiltonian with second-order spin-dependent exchange coupling. From our analysis, we demonstrate how large valley splittings may be achieved and that the valley splitting can be understood with a superexchange mechanism, which strongly depends on the nature of orbital overlap of the transition metal atom with the magnetic atom and the out-of-plane component of the magnetic moment of the magnetic atom. Our calculations provide a basis for understanding prior measurements of valley splitting and suggest routes for enhancing valley splitting in future systems of interest.

I. INTRODUCTION

Two-dimensional (2D) materials have generated great interest in recent years due to their atomically thin structures and highly tunable electronic properties. In particular, monolayer transition metal dichalcogenides (TMDs) with the 2H-MX_2 structure ($M = \text{Mo/W}$, $X = \text{S/Se/Te}$) (Figure 1a) have attracted attention for valleytronics applications due to their semiconducting behavior and the existence of spin-valley coupling in these systems [1]. Monolayer TMDs exhibit a direct band gap [2] located at K and K' in the 2D hexagonal Brillouin zone (Figure 1b,c) where the valence band maximum (VBM) and conduction band minimum (CBM) states are energetically degenerate but inequivalent. Loss of inversion symmetry and strong spin-orbit coupling (SOC), which leads to splitting of the valence and conduction bands at K and K' , give rise to degenerate but inequivalent valleys, which are linked by time reversal symmetry (Figure 1c). The symmetry and strong SOC lead to substantial spin-valley coupling, and the bands at K and K' exhibit opposite spin character and can be selectively excited with left-handed or right-handed circularly polarized light, for K and K' respectively [1].

The energetic degeneracy of the K and K' valleys can be lifted by breaking time reversal symmetry, causing valley polarization, with the band gap isolated in one valley (Figure 1c); the valley splitting is defined as the difference between the dipole-allowed band gaps at K and K' . Valley splitting has been demonstrated experimentally for monolayer TMDs in the presence of external magnetic

fields or when supported by magnetic substrates, where photoluminescence, optical absorption, and reflectance measurements with circularly polarized light confirm that the band gaps in each valley differ when time reversal symmetry is broken [3–9]. Whereas static magnetic fields have been shown to produce relatively modest valley splittings $0.1\text{--}0.22\text{ meV/T}$ [3–6], magnetic substrates such as EuO , EuS , CrI_3 , and ferromagnetic metals Ni/Co lead to valley splittings of $1\text{--}16\text{ meV}$, at least an order of magnitude larger [7–10]. Despite a growing number of experimental reports, a detailed quantitative picture of the origin of the valley splitting associated with magnetic substrates is still lacking. Prior studies have modelled the effect of magnetic substrates using an effective Zeeman field, adding other perturbations to account for inconsistencies between a purely Zeeman-like effect and first-principles calculations [9–12]. Other studies have described the TMD-magnetic atom interaction as magnetic exchange coupling or referred to it as a proximity exchange effect without providing an orbital- or spin-based mechanistic understanding of its nature or magnitude [8, 11, 13, 14]. Ref. [15] qualitatively assesses the impact of Cr-W alignment in a $\text{WSe}_2+\text{CrI}_3$ heterostructure but does not offer a theoretical framework within which to interpret their results. A detailed framework for understanding and quantifying the magnetic exchange coupling generated by orbital hybridization effects and the magnetic moment of the magnetic atom in the substrate, and for suggesting alternative magnetic substrates that might enhance the valley splitting would clearly be of value for interpreting future studies and for applications.

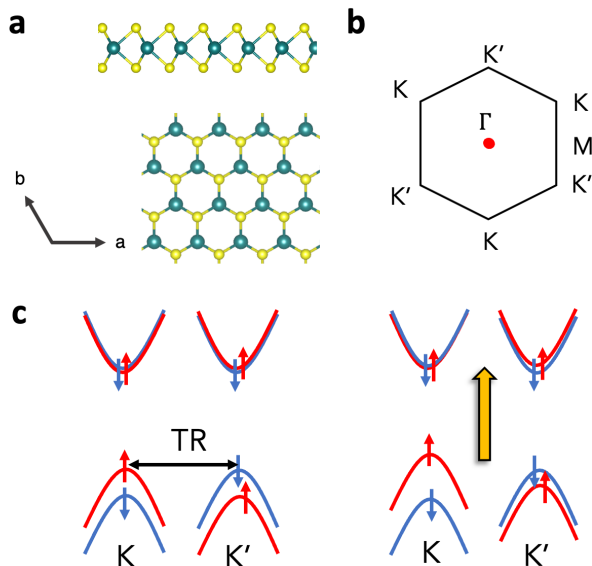


FIG. 1. (a) Side and top view of a monolayer TMD crystal structure with the transition metal in turquoise and the chalcogen in yellow (b) Diagram of hexagonal 2D Brillouin zone (c) Spin-valley coupled valence and conduction bands at K and K' without (left) and with (right) time-reversal symmetry breaking because of a magnetic field (yellow arrow) or magnetic substrate.

In this work we perform a systematic study of valley splitting induced in TMDs by monolayers of suspended magnetic atoms using density functional theory (DFT) calculations. By varying the coverage, alignment, proximity, and magnetic moment of Fe, Co, and Zn atoms on WSe_2 and MoS_2 TMD monolayers, we quantify the importance of these factors to the magnitude of valley splitting, specifically tracking the effect on the top-most valence band eigenvalue splitting at K and K' . We use the results of our DFT calculations to validate a minimal model of valley splitting, fitting our DFT results to a second-order expression from a model Hamiltonian with spin-dependent exchange coupling. From our calculations and analysis, we provide general design principles toward optimal magnetic substrates for large valley splittings and future valleytronics interfaces.

II. METHODS

First-principles calculations are performed using density functional theory (DFT) with a plane-wave basis and projector augmented wave (PAW) pseudopotentials [16] as implemented in the Vienna ab-initio Simulation Package (VASP) [17, 18]. The electrons treated explicitly as valence electrons are $5s^25p^66s^25d^4$ for W, $4s^24p^4$ for Se, $4s^24p^65s^24d^4$ for Mo, $3s^23p^4$ for S, $3s^23p^64s^23d^6$ for Fe, $3s^23p^64s^23d^4$ for Cr, and $3s^23p^64s^23d^{10}$ for

Zn. Monolayer WSe_2 and MoS_2 are relaxed using the generalized-gradient approximation (GGA) as implemented by Perdew, Burke, and Ernzerhof (PBE) [19]; van der Waals dispersion corrections are approximately included using the Grimme-D3 method [20]. The relaxed lattice parameters are 3.29 Å and 3.16 Å respectively, in excellent agreement with experimental values of 3.282 Å [21] and 3.15 Å [22]. For relaxations of monolayer TMDs, an energy cutoff of 1000 eV is used with a $25 \times 25 \times 1$ Γ -centered k -grid. Structures are relaxed until forces are less than 1 meV/Å. Calculations for 100% coverage of Fe atoms are conducted using a 1000 eV energy cutoff and a $25 \times 25 \times 1$ Γ -centered k -grid. Calculations for 33% coverage of Fe atoms are conducted using a 750 eV energy cutoff and a $15 \times 15 \times 1$ Γ -centered k -grid. Non-collinear calculations with spin orbit coupling (SOC) are implemented self-consistently for structural relaxations and charge density generation for band structures. The magnetic moments of the magnetic atoms (Fe, Cr, Zn) are oriented in the positive z direction, unless specified otherwise. A vacuum layer ≥ 20 Å in the c -direction is used to prevent interactions between neighboring monolayers. To ensure that the valence band eigenvalues are not affected by spurious shifts in the Fermi energy, the electrostatic potential is calculated along the c -direction for each TMD+Fe system and the valence band eigenvalues are aligned to vacuum so they are all reported relative to the same absolute energy scale. Testing of the effect of an effective Hubbard U for Fe d states is performed using the PBE+ U method of Dudarev [23].

III. MODEL TMD+FE MONOLAYER SYSTEM BAND STRUCTURE AND EIGENVALUES

We perform DFT calculations for monolayers of Fe atoms at a fixed height z above the surface of WSe_2 and MoS_2 (Figure 2d,e). While Fe atoms could be deposited on monolayer TMDs, we are unaware of any such experiments and we treat this as a model material system for purposes of understanding. We systematically compute the valley splitting as we vary the vertical height (or separation) and lateral alignment of the Fe atoms relative to the TMD substrate; we also consider two different Fe atom coverages. As we use periodic boundary conditions, the Fe atoms constitute a uniform monolayer for a fixed coverage in our calculations. The Fe monolayers are initially laterally aligned such that each of the Fe atoms lies directly above a metal site, either W or Mo in this case. Two coverages are considered: one Fe for 33% of the W or Mo atoms and one for 100%, respectively. Unless specified otherwise, the magnetic moment of the Fe atoms is aligned along the z direction in our calculations, normal to the TMD substrate.

Our calculations show Fe atom coverage-dependent valley splitting which is visible in the computed band structure of the TMD+Fe system (Figure 2b,c). Minimally-dispersive bands with Fe character appear in

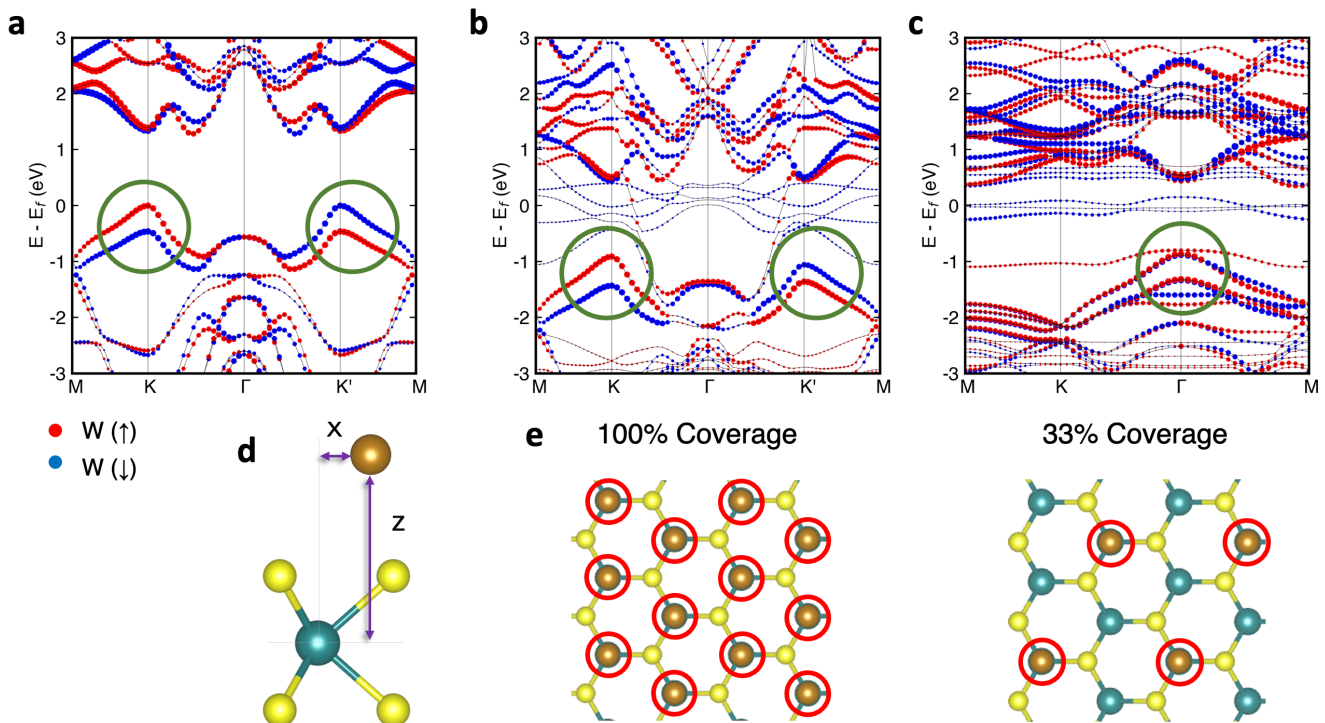


FIG. 2. (a) The band structure of pristine WSe_2 with the spin character of W in each state indicated in red and blue for positive and negative respectively (b) The band structure of WSe_2 with 100% coverage of Fe atoms that are 4.4 \AA above the W atom, with valley splitting clearly visible. (c) The band structure of WSe_2 with 33% coverage of Fe atoms that are 4.4 \AA above the W atom, with K and K' folded into Γ (d) Schematic of Fe atoms above TMD monolayer indicating x and z displacements (e) Schematic of Fe atoms above TMD monolayer at 100% coverage (left) and 33% coverage (right).

the band structure between the TMD valence and conduction bands in this model system, with limited hybridization with W orbitals and reduced dispersion with decreasing Fe coverage.

We identify and track the TMD valence and conduction bands via element-specific orbital projections in a manner we elaborate on below. As height z between the Fe monolayer and the TMD is reduced, the valley splitting systematically increases until at very close distances (small z), significant orbital hybridization dramatically alters the orbital character of the valleys at K and K' , eliminating their desirable symmetry properties (valley degree of freedom and selection rules). We track the shift in the valence band (VB) energies of the TMD, reporting our calculated values in Figure 3 for both 100% coverage (1 Fe per TMD primitive cell) and 33% coverage (1 Fe per $\sqrt{3} \times \sqrt{3}$ TMD supercell, see Figure 2e). Notably, the (111) planes of many perovskite-based oxides have similar lattice parameters to $\sqrt{3} \times \sqrt{3}$ supercells of S and Se TMDs. For example, the hexagonal (111)-plane of BiFeO_3 contains a single Fe atom with an in-plane lattice parameter of 5.58 \AA [24], only 2% different from 5.70 \AA , the in-plane lattice parameter of a $\sqrt{3} \times \sqrt{3}$ supercell of WSe_2 [21]. Thus 33% coverage is a good approximation to the coverage expected for a TMD + (111) mag-

netic oxide heterostructure, a promising avenue of future investigation for valleytronics heterostructures.

We define valley splitting, ΔE_g , as the difference between the dipole-allowed single-particle band gaps at K and K' , $E_g(K)$ and $E_g(K')$, respectively, which are the energies associated with the vertical transitions between the top-most valence band (VB) and the lowest conduction band (CB) eigenvalues of the same spin (the lowest conduction band eigenvalue for MoS_2 and the second lowest conduction band eigenvalue for WSe_2). That is, we define

$$\Delta E_g = E_g(K') - E_g(K), \quad (1)$$

where

$$E_g(K) = E_{K\uparrow}^{CB} - E_{K\uparrow}^{VB} \quad (2)$$

and

$$E_g(K') = E_{K'\downarrow}^{CB} - E_{K'\downarrow}^{VB}, \quad (3)$$

with the spin index on $E_{K/K'}^{VB/CB}$ denoting the spin of the removed electron.

In a $\sqrt{3} \times \sqrt{3}$ supercell of a monolayer TMD, K and K' fold onto the Γ point of the corresponding BZ. The

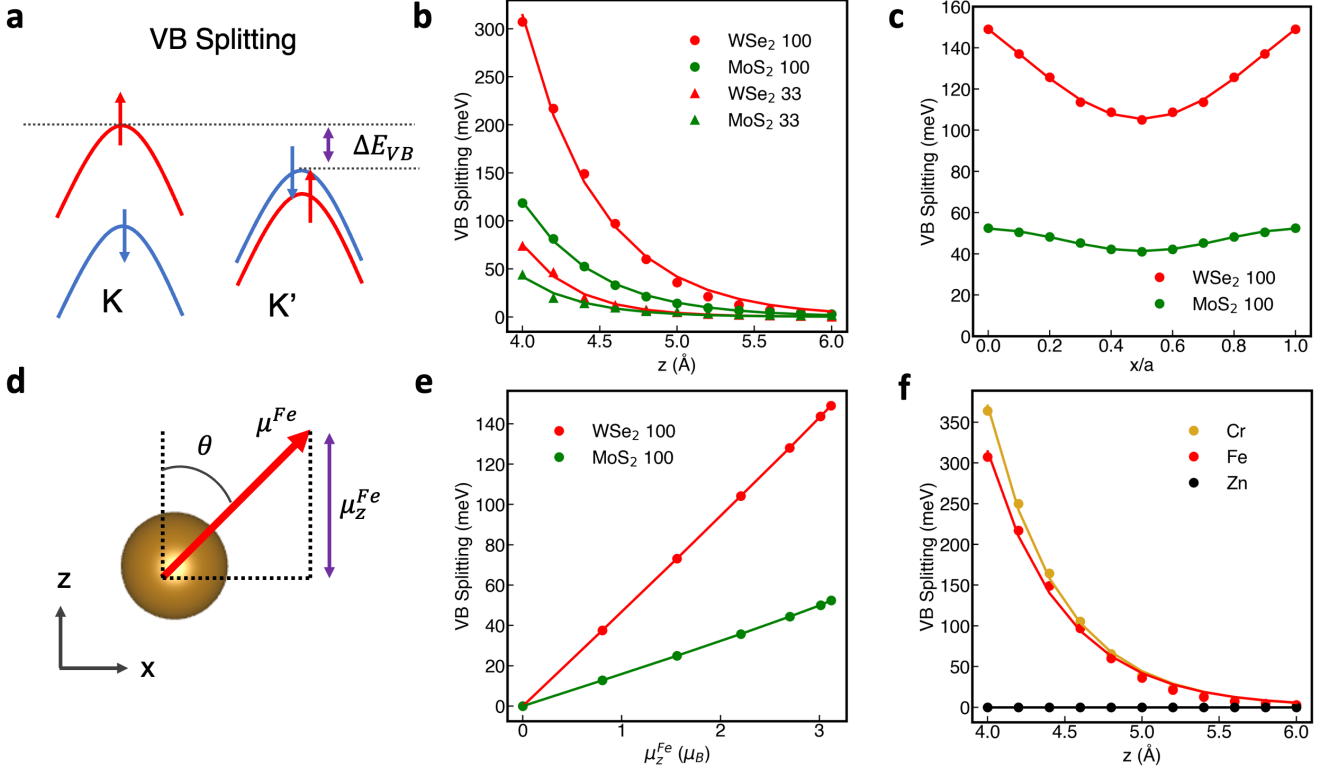


FIG. 3. (a) Schematic illustrating definition of the valence band (VB) splitting (b) Valence band splitting of WSe₂ and MoS₂ with Fe atom at 100% and 33% coverage at variable Fe-W separations z . Circles and triangles are data points, solid lines are exponential fits. (c) Valence band splitting of WSe₂ and MoS₂ with Fe atom at 100% coverage with variable lateral position x and with z fixed at 4.4 Å. Lateral position is represented here as a fractional position along the a -axis (x/a) following the direction of the a -axis displayed in (Figure 1a). Circles are data points, solid lines are fits to cosines. (d) Schematic of canted Fe atom spin and definition of z component of magnetic moment. (e) Valence band splitting of WSe₂ and MoS₂ at 100% coverage with the magnetic moment of the Fe atom at variable angles with respect to the c axis, causing the z component of the magnetic moment to take different values. Circles are data points, solid lines are linear fits. (f) Valence band splitting of WSe₂ in the presence of different magnetic atoms, Fe, Cr and Zn. Circles are data points, solid lines are exponential fits.

contributions from K and K' can be disentangled by projecting out the spin and spherical harmonic character of each band, which together create a unique signature. The VBMs of WSe₂ at K and K' are dominated by a combination of d_{xy} and $d_{x^2-y^2}$ orbital character [11, 15, 25–27] where the x and y Cartesian directions are taken to be in-plane, from which the Mo/W states can be uniquely decomposed into Y_2^{+2} and Y_2^{-2} character at K and K' respectively (see Supplementary Material Figure S1a [28]). Here Y_l^m refers to the spherical harmonic function with orbital angular momentum quantum number l and orbital angular momentum magnetic quantum number m . The CBMs consist predominantly of d_{z^2} W/Mo orbitals which cannot be distinguished between K and K' because $m = 0$ for these orbitals; however, there are additional contributions from Se/S p_x and p_y orbitals which lend unique Y_1^{-1} and Y_1^{+1} character to the CBM at K and K' respectively (see Supplemental Material Figure S1b [28]).

In what follows, we define the valence band (VB) split-

ting, ΔE_{VB} , as the difference between the topmost valence band at K and the topmost valence band at K' (see Fig. 3a), i.e.,

$$\Delta E_{VB} = E_{K\uparrow}^{VB} - E_{K'\downarrow}^{VB}. \quad (4)$$

This difference dominates the valley splitting for the monolayer TMDs considered here, generally deviating from the valley splitting itself by just a minimal amount for these systems (see Supplementary Material Figure S2 [28]), and thus will be used as a proxy for the valley-splitting, ΔE_g , in the discussion that follows.

IV. VALENCE BAND SPLITTING

The calculated VB splitting decays exponentially with increasing height (z) (Figure 3b, see semi-log plot in Supplementary Material Figure S3 [28]) and varies sinusoidally with horizontal displacement (x) (Figure 3c). The nature of the variation of the splitting with height

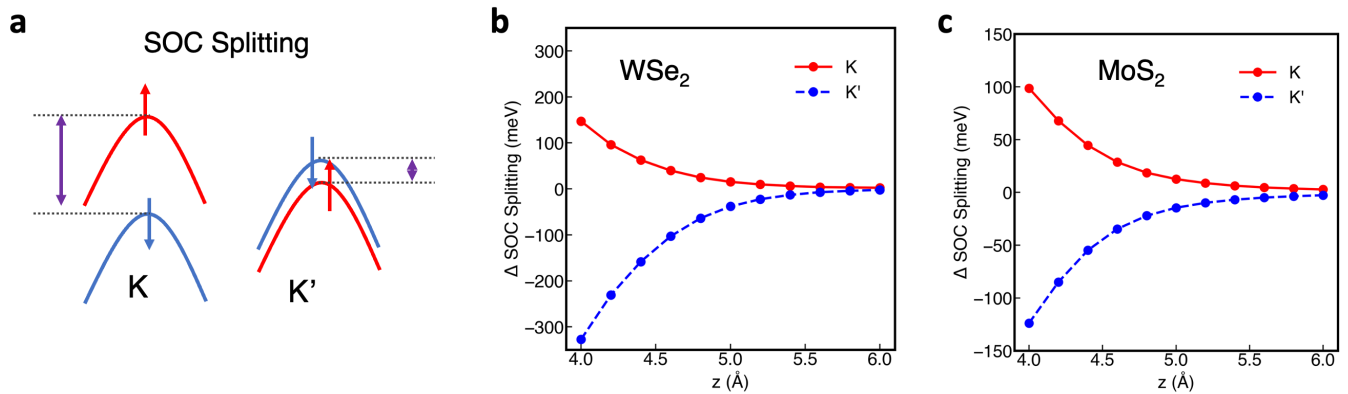


FIG. 4. (a) Schematic of spin-orbit coupling (SOC) splitting at K and K' of TMD valence bands in the presence of Fe atom (b) Change in SOC splitting at K and K' relative to no Fe system for WSe_2 +Fe atom system at 100% coverage and Fe directly above W with interpolation between data points. The absolute value of the SOC splitting in the absence of Fe is 459 meV. (c) Change in SOC splitting at K and K' relative to no Fe system for MoS_2 +Fe atom system at 100% coverage and Fe directly above Mo. The absolute value of the SOC splitting in the absence of Fe is 146 meV. See Supplementary Material for plots of absolute SOC splitting (Figure S5) [28]

and lateral displacement reflects the important role of orbital overlap and hybridization between Fe and TMD states near the VBM on valley splitting, as has also been reported elsewhere for WSe_2 + CrI_3 heterostructures [15]. At small separations, ~ 4 Å, for 100% coverage of Fe atoms directly aligned over WSe_2 , the calculated VB splitting is more than 300 meV, much larger than prior experimental reports of 1-16 meV [7–10], indicating that under more optimal conditions giant valley splittings are possible.

The maximum valley splitting values we report here for our model TMD+Fe system are, depending on the Fe atom height, between one and two orders of magnitude larger than those reported in prior experiments on TMDs supported by magnetic substrates [3–10], and greater than any value yet reported experimentally or theoretically. In one prior first-principles study, the equilibrium W-Eu separation of WSe_2 +EuS with a Eu-terminated surface was computed to be ~ 4.4 Å with $\sim 1:3$ coverage of Eu:W, leading to a predicted valley splitting of 8 meV [9]. Notably, at 100% Fe coverage and at a height of 4.4 Å we compute VB splittings of 148 meV and 52 meV for WSe_2 and MoS_2 respectively, with lateral W/Mo-Fe misalignment resulting in a maximum reduction of 29% and 21%, respectively, in the VB splitting. Should that be achievable experimentally, these VB splittings would be larger than any values yet observed. From the trends in valley splitting we compute here, we can rationalize lower values reported in prior theoretical and experimental work as resulting from imperfect lateral alignment and differing heights and orbital localization, depending on the magnetic atom and substrate. For example, Although the magnetic Eu atoms in EuS have more localized f orbitals and a different ionic radius, for comparison at this W/Mo-Fe separation of 4.4 Å and coverage of 33%, we compute VB splittings of 20 meV and 14 meV, compar-

able numbers given the differences between Fe d and Eu f states and that the Eu-W alignment is not optimal [9]. To further illustrate the sensitivity of VB splitting to orbital overlap, we introduce a Hubbard U [23] for the Fe 3d states to compute the VB splitting, and find that it decreases from 148 meV for $U = 0$ to 60 meV for $U = 7$ eV (see Supplementary Material Figure S4 [28]) for WSe_2 with 100% coverage of Fe atoms at a separation of 4.4 Å.

We note that the VB splitting is also sensitive to the magnitude and orientation of the Fe magnetic moment. Systematically rotating the Fe moment clockwise off the z axis towards the x axis (Figure 3d), the VB splitting for WSe_2 and MoS_2 at 100% coverage at a fixed height of 4.4 Å is computed to decrease linearly with the z component of the magnetic moment of the Fe atom (Figure 3e). Replacing Fe with Cr in the 100% coverage case on WSe_2 , we also observe a similar exponential decay with increasing z and similar dependence on magnetic moment (Figure 3f). Our DFT-PBE magnetic moment of Cr ($3.7 \mu_B$) is larger than the magnetic moment of Fe ($3.1 \mu_B$). The ratios of the VB splitting to the magnetic moment of Cr and Fe differ by only 2%, further validating the linear relationship between out-of-plane magnetic moment and VB splitting. The trend for Cr can be directly related to experimental results for the WSe_2 + CrI_3 heterostructure. In our work the VB splitting predicted for WSe_2 +Cr at the maximum W-Cr separation considered (6 Å) is 2.4 meV. Estimating the coverage of Cr atoms to W atoms to be 50% based on their respective lattice parameters we would expect the VB splitting to be ~ 1 meV. Prior first-principles calculations have predicted a W-Cr distance of 6.8 Å in this heterostructure [15], larger than our maximum value, but similar. Experimental studies have measured a valley splitting of 1-2 meV [8], very close to what our calculations would predict. Finally, as a sanity check, we confirm closed shell Zn, which has no

magnetic moment, does not produce any VB splitting.

An asymmetry arises in the SOC splitting (Figure 4a) at K and K' with the presence of the Fe atoms; the Fe spin inducing valence band splitting does not affect K and K' equally and oppositely. The change in the SOC splitting at K induced by Fe can be expressed as

$$\Delta E_{VB}^{SOC} = (E_{K\uparrow}^{VB} - E_{K\downarrow}^{VB})_{TMD+Fe} - (E_{K\uparrow}^{VB} - E_{K\downarrow}^{VB})_{TMD}, \quad (5)$$

with an analogous expression for the change in the SOC splitting at K' . Going forward we drop the VB subscript used in Eq. 4 since all eigenvalues considered will be VB eigenvalues. For both WSe₂ and MoS₂ the change in the SOC splitting with Fe is significantly greater at K' than at K (Figure 4b,c), by a factor of two for WSe₂ for Fe magnetic moments oriented away from the TMD.

V. SUPEREXCHANGE MODEL HAMILTONIAN

To better understand our DFT calculations, we consider perturbative corrections to the TMD eigenvalues associated with TMD W/Mo-Fe d orbital overlap. For this analysis, we use a model interacting Hamiltonian, H , with an off-diagonal coupling, H_{TMD+Fe} , written as

$$H = \sum_{\mathbf{k}\sigma} \epsilon_{n\mathbf{k}\sigma} c_{n\mathbf{k}\sigma}^+ c_{n\mathbf{k}\sigma} + \sum_{\sigma} \epsilon_{Fe,\sigma} c_{Fe,\sigma}^+ c_{Fe,\sigma} + H_{TMD+Fe} \quad (6)$$

where $\epsilon_{n\mathbf{k}\sigma}$ are the TMD eigenvalues at a given band n , \mathbf{k} -point \mathbf{k} , and spin state σ ; $\epsilon_{Fe,\sigma}$ are the Fe eigenvalues; and c^+ and c are one-electron creation and annihilation operators for the TMD Bloch states (parametrized by band index n , \mathbf{k} -point \mathbf{k} and spin state σ) and localized Fe states with spin state σ [29, 30].

In what follows, we take the dilute monolayer limit and treat the Fe atom and its orbitals and spin state as localized, neglecting any coupling between Fe atoms. We focus on a term representing the interaction between an approximately half-filled Fe atom and a single spin on a Bloch state, i.e.,

$$H_{TMD+Fe} = \sum_{\mathbf{k}\mathbf{k}'\sigma\sigma'} J_{\mathbf{k}\mathbf{k}'} c_{n\mathbf{k}\sigma}^+ c_{n\mathbf{k}'\sigma'} c_{Fe,\sigma'}^+ c_{Fe,\sigma}, \quad (7)$$

where $J_{\mathbf{k}\mathbf{k}'}$ is a set of matrix elements involving overlaps between Fe orbitals and TMD Bloch states and spin indices on $J_{\mathbf{k}\mathbf{k}'}$ have been omitted for simplicity (see Supplementary Material for details [28]). These $J_{\mathbf{k}\mathbf{k}'}$ will be treated as parameters in what follows, and set the energy scale for the effective exchange interaction. It should be noted that this coupling term is not the only possible coupling that may arise between the TMD and Fe atom. We expect additional terms, such as a Hartree term, to arise as well. However, the H_{TMD+Fe} used in this work

is the largest expected coupling contribution that affects K and K' differently, as will be seen in the following analysis. Since our objective is ultimately to model the difference between the eigenvalues at K and K' , we neglect discussion of other coupling terms.

Our first-principles calculations show proximity to spin-up Fe electrons decreases the energy of the spin-down TMD eigenstate at K' and increases the energy of the spin-up TMD eigenstate at K . For this to be consistent with the above interaction Hamiltonian, the matrix elements $J_{\mathbf{k}\mathbf{k}'}$ must promote an antiferromagnetic interaction leading us to conclude the $J_{\mathbf{k}\mathbf{k}'}$ which appear above are not related to direct exchange, which would have the wrong sign for $J_{\mathbf{k}\mathbf{k}'}$, but rather a superexchange mechanism. Our focus on this term has analogies with Anderson's analysis of half-filled d orbitals interacting with one another where the dominant second-order term in the kinetic and ionic potential energy represents double-hopping, or superexchange [29]. The difference here is that one of the spins, associated with the Fe atom, is localized in real space; the other, associated with a TMD Bloch function at K or K' , is localized in reciprocal space. We write the eigenstates of the uncoupled TMD+Fe system as tensor products of TMD Bloch states and localized Fe spin states $|n\mathbf{k}\sigma\rangle \otimes |Fe, \sigma\rangle = |n\mathbf{k}\sigma; \sigma_{Fe}\rangle$. We simplify this further by treating the Fe atom spins as a single unit with total spin S and total spin magnetic quantum number M_s^{Fe} so that our states can be labeled as $|n\mathbf{k}\sigma; M_s^{Fe}\rangle$.

Treating H_{TMD+Fe} in Eq. 6 as a perturbation to the TMD VB eigenvalues at K and K' , the corrected eigenvalues to second order become:

$$E_{K\uparrow} = E_{K\uparrow}^0 + M_s^{Fe} J_{KK} + \sum_{\mathbf{k}'} |J_{K\mathbf{k}'}|^2 \left[\frac{(M_s^{Fe})^2}{E_{K\uparrow} - E_{\mathbf{k}'\uparrow}} + \frac{S(S+1) - M_s^{Fe}(M_s^{Fe} + 1)}{E_{K\uparrow} - E_{\mathbf{k}'\downarrow}} \right] \quad (8)$$

and

$$E_{K'\downarrow} = E_{K'\downarrow}^0 - M_s^{Fe} J_{K'K'} + \sum_{\mathbf{k}'} |J_{K'\mathbf{k}'}|^2 \left[\frac{(M_s^{Fe})^2}{E_{K'\downarrow} - E_{\mathbf{k}'\downarrow}} + \frac{S(S+1) - M_s^{Fe}(M_s^{Fe} - 1)}{E_{K'\downarrow} - E_{\mathbf{k}'\uparrow}} \right] \quad (9)$$

where M_s^{Fe} and S are taken to be $\frac{3}{2}$, based on the calculated DFT-PBE value of the magnetic moment of the Fe atom ($3.1 \mu_B$) and assuming a gyromagnetic ratio of $\gamma \approx 2$. It should again be noted that there should be further corrections arising from other coupling interactions, but that those interactions are expected to produce identical corrections to the eigenvalues at K and K' .

In principle, the \mathbf{k} -dependence of $J_{\mathbf{k}\mathbf{k}'}$ will be related to details of the overlap between the itinerant Bloch TMD states and localized Fe states. Since the TMD VB eigenfunctions at K and K' differ only by a phase, consisting of contributions from 5d/4d orbitals with spherical harmonics Y_2^{+2} and Y_2^{-2} respectively (see Supplementary Material Figure S1 [28]), we expect $J_{KK} = J_{K'K'} = J$. To

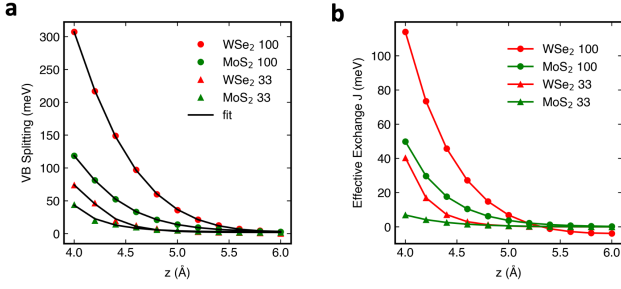


FIG. 5. (a) Valence band splitting for WSe₂ and MoS₂ for 100% coverage and 33% coverage (with the Fe atoms positioned directly on top of the W and Mo atoms), same as Fig. 3b, and fits to the valence band splitting model (b) Fitted values of effective exchange J arising from the superexchange interaction for WSe₂ and MoS₂ for 100% and 33% coverage.

further simplify as much as possible, we assume minimal \mathbf{k} -dependence of $J_{\mathbf{k}\mathbf{k}'}$ near K and K' , and approximate that $J_{K\mathbf{k}'} \approx J_{KK}$ and $J_{K'\mathbf{k}'} \approx J_{K'K'}$, with contributions from neighboring \mathbf{k} points weighted by how similar their wave functions are to those of the VBM at K and K' , equivalently $J_{K\mathbf{k}'} = Jw(\mathbf{k}')$ and $J_{K'\mathbf{k}'} = Jw(\mathbf{k}')$ (see Supplementary Material for details of these approximations [28]). This is a reasonable assumption because the orbital character in the neighboring Bloch states in the top and bottom TMD VBs consist predominantly of 5d/4d orbitals with Y_2^{+2} and Y_2^{-2} spherical harmonics. With these approximations, we can pull J out of the summations, and define the constants

$$\alpha = \sum_{\mathbf{k}'} \frac{w(\mathbf{k}')}{E_{K\uparrow} - E_{\mathbf{k}'\uparrow}} = \sum_{\mathbf{k}'} \frac{w(\mathbf{k}')}{E_{K'\downarrow} - E_{\mathbf{k}'\downarrow}} \quad (10)$$

and

$$\beta = \sum_{\mathbf{k}'} \frac{w(\mathbf{k}')}{E_{K\uparrow} - E_{\mathbf{k}'\downarrow}} = \sum_{\mathbf{k}'} \frac{w(\mathbf{k}')}{E_{K'\downarrow} - E_{\mathbf{k}'\uparrow}} \quad (11)$$

for the same-spin and spin-flip summations over the top VB and bottom VB respectively.

It follows from these approximations that an asymmetry in the magnitude of the valence band eigenvalue shifts at K and K' arises at second order. Capturing this asymmetry is necessary to rationalize the manner in which the VB SOC splitting (top VB minus bottom VB, Figure 4a) changes with z (Figure 4b). To first order in J , equal and opposite changes in the SOC splitting would be expected. However, the first order term alone cannot lead to the valence band splitting seen in our DFT calculations. From our model, the second-order terms in J lead to the asymmetry in this splitting, and hence the valley splitting at lowest order (see Supplementary Material for further details [28]).

To understand the trends in the VB splitting predicted by this model, we take the difference between the two

perturbed eigenvalues, ΔE_{VB} , which reduces to

$$\Delta E_{VB} = E_{K\uparrow} - E_{K'\downarrow} = 2M_s^{Fe}(J - J^2\beta). \quad (12)$$

When the magnetic impurity spin is canted by an angle θ away from the z axis and clockwise towards the x axis (Figure 3d), $|\mathbf{k}\sigma; M_s^{Fe}\rangle \rightarrow e^{-iS_y\theta} |\mathbf{k}\sigma; M_s^{Fe}\rangle$ and the corresponding expression for the VB splitting is modified to (see Supplementary Material for derivation details [28])

$$\Delta E_{VB} = E_{K\uparrow} - E_{K'\downarrow} = 2M_s^{Fe} \cos\theta(J - J^2\beta). \quad (13)$$

Here $2M_s^{Fe} \cos\theta$ corresponds to the z component of the Fe magnetic moment μ_z^{Fe} .

From our DFT calculations, we know J to be sensitive to both the height z and the lateral alignment. As J involves matrix elements between Fe and TMD states with dominant Fe and Mo/W d atomic orbital character we assume J to have the form

$$J(z) = ae^{-bz}f(z) \quad (14)$$

where $f(z)$ is a polynomial, a generic form consistent with the relevant states being hydrogenic 3d and 5d/4d atomic orbitals, respectively.

We fit Eqs. 13 and 14 to the DFT-PBE VB eigenvalue splitting (Fig. 3b, 5a) as a function of vertical displacement z for WSe₂ and MoS₂ at 100% and 33% coverage.

From Figure 5b we see that WSe₂ exhibits a larger J than MoS₂ at a given separation, consistent with 5d orbitals having a greater spatial extent than 4d orbitals. The J calculated here contains an implicit dependence on the coverage of the magnetic atoms. For both WSe₂ and MoS₂, J for the 100% coverage case is 6 times larger than J for the 33% coverage case at a relevant height z of 4.4 Å, larger than the expected factor of 3 assuming a linear dependence on coverage. This may be because for the 100% coverage case, each Mo and W could potentially interact with neighboring Fe atoms, beyond the one that is aligned directly above the transition metal. It could also be associated with dispersion and \mathbf{k} -dependence of the Fe states, which is neglected in our model. Nevertheless, this second-order superexchange model captures the trends exceedingly well, allowing us to use this for intuition in the future design of valleytronics interfaces.

VI. DISCUSSION

Based on these results and our model, we can summarize general principles that can guide development of optimal magnetic substrates for large valley splitting and valleytronics applications. First, the vertical proximity (z) between the W/Mo ion and the magnetic atom in the substrate must be reduced as much as possible while keeping the valley degree of freedom in the TMD intact. Reducing the distance between the TMD transition metal (W/Mo) and the magnetic atom in the magnetic substrate could be achieved, for example, by using magnetic

substrates that are terminated by the magnetic atom. Because of the exponential nature of this effect, 1 Å of additional distance between a magnetic atom and the TMD transition metal atom due to the addition of, for example, oxygen on the surface can reduce the valley splitting by an order of magnitude.

Second, lateral alignment (x) of the TMD transition metal (W/Mo) with the magnetic atom must be optimized. This can be achieved by identifying magnetic substrates with good lattice parameter matching to the selected TMD. Although important, lateral alignment is not as sensitive as the vertical proximity as it only leads to a sinusoidal variation in valley splitting, decreasing it by $\sim 20\%$ at maximal misalignment. In prior experimental studies of TMDs with substrates like EuS and CrI₃, the small valley splitting, ~ 1 -16 meV, can be understood by considering the low coverage and significant lattice parameter mismatch, leading to poor alignment of the W/Mo atoms with the magnetic Eu and Cr atoms. As previously discussed, perovskite-related magnetic oxides may offer better lattice alignment and coverage, and therefore are an avenue worth further study.

Third, we find that the out-of-plane magnetic moment of the magnetic atom must be maximized. This can be achieved by tuning the chemical identity, oxidation state, or local environment of the magnetic atom so that it has a larger magnetic moment and out-of-plane easy axis. It should be noted that this requirement is not as critical as the proximity requirements; valley splitting only decreases linearly with decreasing out-of-plane magnetic moment, not exponentially. This indicates that even substrates with canted magnetic moments could still produce valley splitting, so long as the proximity and alignment of the magnetic atoms to the W/Mo atoms is optimized.

Fourth, maximizing the radial extent of the TMD transition metal and the magnetic atoms will amplify the effective exchange J which increases with increasing orbital overlap, or equivalently, with increasing radial extent of both the TMD Bloch state (dominated by the transition metal W/Mo) and the magnetic atom. Since the valence

band splitting increases with increasing J , this implies that valley splitting can be maximized by using larger transition metals in the TMD (W) and by using magnetic substrates with magnetic atoms that have larger radial extent.

VII. CONCLUSION

Motivated by recent experiments, and using first-principles density functional theory calculations, we have studied in detail trends in valley splitting of monolayer TMDs with the proximity, alignment, and coverage of overlayers of magnetic atoms. We find large valley splittings for optimal geometries in which magnetic atoms are well aligned sitting atop each TMD TM atom that are one to two orders of magnitude larger than previously reported. Our analysis indicates that an orbital overlap-driven superexchange interaction drives valley splitting in TMDs supported by magnetic substrates. By systematically varying the placement and coverage of magnetic atoms at two different coverages, we have pinpointed and explored the differing shifts in the valence band eigenvalues at K and K' giving rise to valley splitting. Through analysis of expressions originating with second-order perturbation theory in a model coupling Hamiltonian between the magnetic atoms and the TMD, we have elucidated the dependence of the valley splitting on the superexchange interaction.

VIII. ACKNOWLEDGEMENTS

This work is supported by the Air Force Office of Scientific Research Hybrid Materials MURI under award number FA9550-18-1-0480. Computational resources were provided by the National Energy Research Scientific Computing Center (NERSC) through the US Department of Energy. Calculations were also performed on the Lawrence Livermore cluster, operated by Lawrence Berkeley National Laboratory.

-
- [1] K. F. Mak, K. He, J. Shan, and T. F. Heinz, Control of valley polarization in monolayer MoS₂ by optical helicity, *Nat. Nanotechnol.* **7**, 494 (2012).
 - [2] K. F. Mak, C. Lee, J. Hone, J. Shan, and T. F. Heinz, Atomically Thin MoS₂: A New Direct-Gap Semiconductor, *Phys. Rev. Lett.* **105**, 136805 (2010).
 - [3] Y. Li, J. Ludwig, T. Low, A. Chernikov, X. Cui, G. Arefe, Y. D. Kim, A. M. van der Zande, A. Rigosi, H. M. Hill, S. H. Kim, J. Hone, Z. Li, D. Smirnov, and T. F. Heinz, Valley Splitting and Polarization by the Zeeman Effect in Monolayer MoSe₂, *Phys. Rev. Lett.* **113**, 266804 (2014).
 - [4] A. Srivastava, M. Sidler, A. V. Allain, D. S. Lembke, A. Kis, and A. Imamoglu, Valley Zeeman effect in elementary optical excitations of monolayer WSe₂, *Nat. Phys.* **11**, 141 (2015).
 - [5] G. Aivazian, Z. Gong, A. M. Jones, R.-L. Chu, J. Yan, D. G. Mandrus, C. Zhang, D. Cobden, W. Yao, and X. Xu, Magnetic control of valley pseudospin in monolayer WSe₂, *Nat. Phys.* **11**, 148 (2015).
 - [6] D. MacNeill, C. Heikes, K. F. Mak, Z. Anderson, A. Kormányos, V. Zólyomi, J. Park, and D. C. Ralph, Breaking of Valley Degeneracy by Magnetic Field in Monolayer MoSe₂, *Phys. Rev. Lett.* **114**, 037401 (2015).
 - [7] C. Zhao, T. Norden, P. Zhang, P. Zhao, Y. Cheng, F. Sun, J. P. Parry, P. Taheri, J. Wang, Y. Yang, T. Scrace, K. Kang, S. Yang, G.-x. Miao, R. Sabirianov, G. Kioseoglou, W. Huang, A. Petrou, and H. Zeng, Enhanced valley splitting in monolayer WSe₂ due to mag-

- netic exchange field, *Nat. Nanotechnol.* **12**, 757 (2017).
- [8] D. Zhong, K. L. Seyler, X. Linpeng, R. Cheng, N. Sivadas, B. Huang, E. Schmidgall, T. Taniguchi, K. Watanabe, M. A. McGuire, W. Yao, D. Xiao, K.-M. C. Fu, and X. Xu, Van der Waals engineering of ferromagnetic semiconductor heterostructures for spin and valleytronics, *Sci. Adv.* **3**, e1603113 (2017).
- [9] T. Norden, C. Zhao, P. Zhang, R. Sabirianov, A. Petrou, and H. Zeng, Giant valley splitting in monolayer WS_2 by magnetic proximity effect, *Nat. Commun.* **10**, 4163 (2019).
- [10] K. Zollner, P. E. Faria Junior, and J. Fabian, Giant proximity exchange and valley splitting in transition metal dichalcogenide/ $h\text{BN}/(\text{Co}, \text{Ni})$ heterostructures, *Phys. Rev. B* **101**, 085112 (2020).
- [11] J. Qi, X. Li, Q. Niu, and J. Feng, Giant and tunable valley degeneracy splitting in MoTe_2 , *Phys. Rev. B* **92**, 121403(R) (2015).
- [12] Y. Ominato, J. Fujimoto, and M. Matsuo, Valley-Dependent Spin Transport in Monolayer Transition-Metal Dichalcogenides, *Phys. Rev. Lett.* **124**, 166803 (2020).
- [13] X. Liang, L. Deng, F. Huang, T. Tang, C. Wang, Y. Zhu, J. Qin, Y. Zhang, B. Peng, and L. Bi, The magnetic proximity effect and electrical field tunable valley degeneracy in MoS_2/EuS van der Waals heterojunctions, *Nanoscale* **9**, 9502 (2017).
- [14] D. Zhong, K. L. Seyler, X. Linpeng, N. P. Wilson, T. Taniguchi, K. Watanabe, M. A. McGuire, K.-M. C. Fu, D. Xiao, W. Yao, and X. Xu, Layer-resolved magnetic proximity effect in van der Waals heterostructures, *Nat. Nanotechnol.* **15**, 187 (2020).
- [15] Z. Zhang, X. Ni, H. Huang, L. Hu, and F. Liu, Valley splitting in the van der Waals heterostructure $\text{WSe}_2/\text{CrI}_3$: The role of atom superposition, *Phys. Rev. B* **99**, 115441 (2019).
- [16] G. Kresse and D. Joubert, From ultrasoft pseudopotentials to the projector augmented-wave method, *Phys. Rev. B* **59**, 1758 (1999).
- [17] G. Kresse and J. Furthmüller, Efficiency of ab-initio total energy calculations for metals and semiconductors using a plane-wave basis set, *Computational Materials Science* **6**, 15 (1996).
- [18] G. Kresse and J. Furthmüller, Efficient iterative schemes for ab initio total-energy calculations using a plane-wave basis set, *Phys. Rev. B* **54**, 11169 (1996).
- [19] J. P. Perdew, K. Burke, and M. Ernzerhof, Generalized Gradient Approximation Made Simple, *Phys. Rev. Lett.* **77**, 3865 (1996).
- [20] S. Grimme, J. Antony, S. Ehrlich, and H. Krieg, A consistent and accurate ab initio parametrization of density functional dispersion correction (DFT-D) for the 94 elements H-Pu, *J. Chem. Phys.* **132**, 154104 (2010).
- [21] W. J. Schutte, J. L. De Boer, and F. Jellinek, Crystal structures of tungsten disulfide and diselenide, *Journal of Solid State Chemistry* **70**, 207 (1987).
- [22] R. G. Dickinson and L. Pauling, The crystal structure of molybdenite, *J. Am. Chem. Soc.* **45**, 1466 (1923).
- [23] S. L. Dudarev, G. A. Botton, S. Y. Savrasov, C. J. Humphreys, and A. P. Sutton, Electron-energy-loss spectra and the structural stability of nickel oxide: An LSDA+U study, *Phys. Rev. B* **57**, 1505 (1998).
- [24] I. Sosnowska, W. Schäfer, W. A. Kockelmann, and I. O. Troyanchuk, Neutron Diffraction Studies of the Crystal and Magnetic Structures of $\text{BiMn}_x\text{Fe}_{1-x}\text{O}_3$ Solid Solutions, *Mater. Sci. Forum* **616**, 378 (2001).
- [25] T. Cao, G. Wang, W. Han, H. Ye, C. Zhu, J. Shi, Q. Niu, P. Tan, E. Wang, B. Liu, and J. Feng, Valley-selective circular dichroism of monolayer molybdenum disulphide, *Nat. Commun.* **3**, 887 (2012).
- [26] D. Xiao, G.-B. Liu, W. Feng, X. Xu, and W. Yao, Coupled Spin and Valley Physics in Monolayers of MoS_2 and Other Group-VI Dichalcogenides, *Phys. Rev. Lett.* **108**, 196802 (2012).
- [27] Q. Zhang, S. A. Yang, W. Mi, Y. Cheng, and U. Schwingenschlögl, Large Spin-Valley Polarization in Monolayer MoTe_2 on Top of $\text{EuO}(111)$, *Advanced Materials* **28**, 959 (2016).
- [28] See Supplementary Material at [URL will be inserted by publisher] for information on spherical harmonics projections, valley splitting vs. valence band splitting, semi-log plot of valence band splitting, effects of Hubbard U on valence band splitting, absolute SOC splitting, valence band eigenvalues, details of second order perturbative approach, details of weighted summations, and derivation of canted spin valence band splitting.
- [29] P. W. Anderson, New Approach to the Theory of Superexchange Interactions, *Phys. Rev.* **115**, 2 (1959).
- [30] G. D. Mahan, *Many-Particle Physics* (Plenum Press, 1981).